Available online at www.sciencedirect.com
ScienceDirect
Journal of Sound and Vibration 325 (2009) 122–144
JOURNAL OF SOUND AND VIBRATION
www.elsevier.com/locate/jsvi

Numerical prediction of aft radiation of turbofan tones through exhaust jets

Y. Özyörük*

Department of Aerospace Engineering, Middle East Technical University, 06531 Ankara, Turkey

Received 15 September 2008; received in revised form 10 March 2009; accepted 11 March 2009
Handling Editor: R.J. Astley
Available online 5 May 2009

Abstract

This paper describes a numerical methodology for calculating tonal noise propagation and radiation through turbomachinery exhaust ducts, including non-uniform background jet flows. The numerical method is based on solution of the linearized Euler equations directly in the frequency domain, employing a direct, sparse matrix solver in parallel. Acoustic sources are introduced into the computational domain via the perfectly matched layer equations. Various test cases including propagation through infinite ducts, and propagation and radiation through semi-infinite ducts with and without liners are solved, and results are compared with analytical solutions. It is demonstrated that solutions even with thin shear layers separating the exterior and jet streams at reasonably high Mach numbers can be obtained quite successfully. The method is also validated by simulating the radiated sound waves from two actual engine exhaust cowl geometries, and the results are compared with experimental data.

1. Introduction

Great advances have been achieved in the past few decades in reducing the overall noise emission from aircraft. Despite this the airline operators and aircraft manufacturers are still under pressure by government agencies and communities living near airports to reduce the noise levels further. Among the dominant noise sources on today's large passenger aircraft is the fan noise radiating both forward and rearward, especially at take off. Before its radiation, this component of noise propagates through the air intake and exhaust nozzles, where part of the acoustic energy is absorbed by the acoustic linings embedded into the duct walls. Successful lining design relies on predicting the modal content and propagation characteristics of this noise.

There are various important aspects in prediction of sound propagation through and radiation from engine exhausts. High speed duct flows make the upstream and downstream running characteristics that carry the acoustic energy quite disparate. Waves spinning and propagating in both directions must be resolved properly by the used numerical method. This requires use of high-order algorithms and efficient numerical filters. Also suitable implementation of the wall condition on the acoustic lining elements is needed. This is achieved for a

*Tel.: +90 312 210 4275; fax: +90 312 210 4250.
E-mail address: yusuf@ae.metu.edu.tr

0022-460X/$ - see front matter © 2009 Elsevier Ltd. All rights reserved.
doi:10.1016/j.jsv.2009.03.012

locally reacting liner by describing its response to the sound field in the frequency domain. This response is communicated with the interior solution using the frequency-domain impedance condition [1]. However, the stability and regularization of this condition under the presence of wall flow is a critical issue which is still subject of research [2,3]. Time-domain computations involving liners and flow require special care and treatment to prevent instability development [4–6]. In contrast, the unstable modes associated with the impedance condition are most often eliminated naturally in a frequency-domain computation without a particular treatment. This is also true [3,7] for the convective, shear layer (Kelvin–Helmholtz, K–H) instabilities [8] that exist inherently in exhaust noise prediction problems. Time-domain simulations of the exhaust noise radiation with the linearized Euler equations (LEE) sometimes fail as a result of the K–H instability waves becoming temporally unbounded. Although it may be possible to suppress these instabilities through some filtering or time-averaging procedures oriented toward the frequency of the sound field, this is not a robust procedure, as the advantage of the time-domain method being able to simulate a broadband source is lost.

Among the approaches to suppress the K–H instability in time-domain simulations of sound propagation through, for example, plug flow jets has been the use of an artificial shear layer concept. The vortex sheet separating the plug flow and the exterior stream is replaced by a gradually growing finite size shear layer. This imitates an actual situation, and consequently a shift in the frequency of the most unstable mode is created [9,10] to prevent the K–H instability. Another approach has been the drop of the mean flow gradients causing the instability from the governing equations [11,12], which usually appears mostly close to the nozzle lip where the shear layer is quite thin.

The above concerns associated with the liners and K–H instabilities that present in an actual exhaust noise radiation problem are alleviated in the present paper by a direct, frequency-domain solution approach. From the same point of view, Zhao and Morris [13] developed a frequency-domain, finite-element LEE solver based on the streamline upwind Petrov–Galerkin (SUPG) scheme for jet and turbofan exhaust problems. Similarly, the present paper develops a frequency-domain code using finite differences. This code is named FLESTURN. In this model the geometry is assumed axisymmetric. Then, for a single spinning mode order the LEE are reduced to a form in which only axial and radial derivatives appear (2.5-D). This form is discretized using high-order differences, and the resulting linear system of equations is solved directly using a parallel, high performance, sparse matrix solver.

In the following sections, the present methodology is described. Then, some simple infinite duct cases are solved at various conditions to quickly verify the developed code. This will be followed by computations of some radiation problems from semi-infinite ducts, including an annular duct with infinite centerbody to which analytical solutions have been recently extended by two research groups [14,15] following Munt's work [16]. The work of Demir and Rienstra [14] can also treat acoustically lined centerbodies beyond the exit of the annulus. By comparing to their hard and lined wall annular duct results, it will be demonstrated that the present LEE solver can handle problems, without much difficulty, even with reasonably high Mach number duct flows and thin shear layers that usually trouble time-domain methods. The code will also be validated by comparing results with the measured data for two engine exhaust configurations.

2. Model development

The geometry of interest is of a typical turbofan exhaust, having a primary flow (core) duct and secondary flow (bypass) duct, as illustrated in Fig. 1. Acoustic waves created in the upstream regions by some mechanisms propagate through these ducts, and then radiate to the far-field through the shear layers emanating from the nozzle trailing edges. The LEE properly account for the refraction and amplification effects of the generally highly non-uniform background flows both in the ducts and jets. Computationally the acoustic modes are introduced in a limited upstream region in the core or bypass duct. The conditions imposed here must allow outgoing waves entirely without reflection or at least absorb them to the extent that the reflected components do not contaminate the physical solution. No boundary conditions truly simulate outgoing wave phenomena. However, as will be illustrated later the recently developed perfectly matched layers (PML) approach of Hu [17] satisfactorily serves to this purpose while simultaneously introducing the

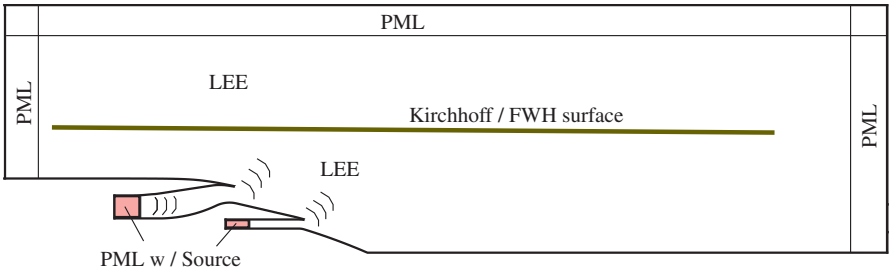

Fig. 1. General configuration.

desired incoming waves. This approach may also be utilized effectively to absorb the outgoing waves in the far-field.

In the following subsections, the governing equations are given first. Then, the boundary conditions for the inlets of the ducts, far-field boundaries, and the duct walls are described. The PML equations that match to the LEE perfectly at an interface between the interior domain and solution layers adjacent to the inlet and far-field boundaries are also given as well as the far-field prediction technique. Finally, various discretization approaches that have been used in the present code development are discussed.

2.1. Governing equations

The 3-D, time-dependent, LEE are transformed into the frequency domain and decomposed into periodic azimuthal modes. This is simply done by assuming the perturbations to the primitive, dependent variables are of the circular frequency ω and of the azimuthal mode order m with the form

$$\mathbf{q}'(\mathbf{x},t) = \mathrm{Re}\{\hat{\mathbf{q}}(x,r,\omega)\mathrm{e}^{\mathrm{i}\omega t+\mathrm{i}m\theta}\}, \tag{1}$$

where

$$\mathbf{q}' = [\rho', u', v', w', p']^{\mathrm{T}}, \quad \hat{\mathbf{q}} = [\hat{\rho}, \hat{u}, \hat{v}, \hat{w}, \hat{p}]^{\mathrm{T}}. \tag{2}$$

Here ρ' is the density perturbation, u' is the axial, v' is the radial, and w' is the azimuthal velocity perturbations in the cylindrical polar coordinate directions (x, r, θ), respectively, p' is the pressure perturbation, $\mathrm{i} = \sqrt{-1}$, ω is the circular frequency, and a hat on a variable indicates a complex quantity. Upon substitution of the above form into the Euler equations linearized about a non-uniform, axisymmetric flow state $\mathbf{q}_0 = [\rho_0, \mathbf{V}_0, p_0]^{\mathrm{T}}$, the equations governing the complex amplitudes of the flow perturbations may be written in cylindrical polar coordinates as

$$\mathbf{A}_{\mathrm{int}}\frac{\partial\hat{\mathbf{q}}}{\partial x} + \mathbf{B}_{\mathrm{int}}\frac{\partial\hat{\mathbf{q}}}{\partial r} + \mathbf{C}_{\mathrm{int}}\hat{\mathbf{q}} = \hat{\mathbf{r}}_{\mathrm{int}}, \tag{3}$$

where the Jacobian matrices $\mathbf{A}$, $\mathbf{B}$, and $\mathbf{C}$ are given by

$$\mathbf{A}_{\mathrm{int}} = \begin{bmatrix} u_0 & \rho_0 & 0 & 0 & 0 \\ 0 & u_0 & 0 & 0 & 1/\rho_0 \\ 0 & 0 & u_0 & 0 & 0 \\ 0 & 0 & 0 & u_0 & 0 \\ 0 & \gamma p_0 & 0 & 0 & u_0 \end{bmatrix}, \quad \mathbf{B}_{\mathrm{int}} = \begin{bmatrix} v_0 & 0 & \rho_0 & 0 & 0 \\ 0 & v_0 & 0 & 0 & 0 \\ 0 & 0 & v_0 & 0 & 1/\rho_0 \\ 0 & 0 & 0 & v_0 & 0 \\ 0 & 0 & \gamma p_0 & 0 & v_0 \end{bmatrix},$$

$$\mathbf{C}_{\text{int}} = \begin{bmatrix} \mathrm{i}\omega + \nabla\cdot\mathbf{V}_0 & \frac{\partial \rho_0}{\partial x} & \frac{\rho_0}{r} + \frac{\partial \rho_0}{\partial r} & \rho_0 \frac{\mathrm{i}m}{r} & 0 \\ -\frac{1}{\rho_0^2}\frac{\partial p_0}{\partial x} & \mathrm{i}\omega + \frac{\partial u_0}{\partial x} & \frac{\partial u_0}{\partial r} & 0 & 0 \\ -\frac{1}{\rho_0^2}\frac{\partial p_0}{\partial r} & \frac{\partial v_0}{\partial x} & \mathrm{i}\omega + \frac{\partial v_0}{\partial r} & 0 & 0 \\ 0 & 0 & 0 & \mathrm{i}\omega + \frac{v_0}{r} & \frac{\mathrm{i}m}{\rho_0 r} \\ 0 & \frac{\partial p_0}{\partial x} & \frac{\gamma p_0}{r} + \frac{\partial p_0}{\partial r} & \gamma p_0 \frac{\mathrm{i}m}{r} & \mathrm{i}\omega + \gamma\nabla\cdot\mathbf{V}_0 \end{bmatrix}, \tag{4}$$

and $\hat{\mathbf{r}}_{\text{int}}$ is a right-hand side source vector that may be introduced in the interior domain. When waves are introduced from a PML, the right-hand side source vector for the interior equations is set to zero.

2.2. Boundary conditions

2.2.1. PML conditions for duct inlet/outlet and far-field

The PML equations of Hu [17] are extended to cylindrical polar coordinates and dimensionalized in a consistent manner to the interior governing equations. Background flow is assumed uniform at the inlets of the ducts, as well as at the far-field boundaries, with only an axial velocity component, $\mathbf{V}_0 = u_0\hat{\mathbf{e}}_x$. The PML equations are written in a similar form to the LEE. Then the Jacobian matrices are given by

$$\mathbf{A}_{\text{pml}} = \begin{bmatrix} u_0\left(1+\frac{\sigma_r}{\mathrm{i}\omega}\right) & \rho_0\left(1+\frac{\sigma_r}{\mathrm{i}\omega}\right) & 0 & 0 & 0 \\ 0 & u_0\left(1+\frac{\sigma_r}{\mathrm{i}\omega}\right) & 0 & 0 & \left(1+\frac{\sigma_r}{\mathrm{i}\omega}\right)/\rho_0 \\ 0 & 0 & u_0\left(1+\frac{\sigma_r}{\mathrm{i}\omega}\right) & 0 & \left(1+\frac{\sigma_x}{\mathrm{i}\omega}\right)/\rho_0 \\ 0 & 0 & 0 & u_0\left(1+\frac{\sigma_r}{\mathrm{i}\omega}\right) & 0 \\ 0 & \gamma p_0\left(1+\frac{\sigma_r}{\mathrm{i}\omega}\right) & 0 & 0 & u_0\left(1+\frac{\sigma_r}{\mathrm{i}\omega}\right) \end{bmatrix},$$

$$\mathbf{B}_{\text{pml}} = \begin{bmatrix} 0 & 0 & \rho_0(1+\frac{\sigma_x}{\mathrm{i}\omega}) & 0 & 0 \\ 0 & 0 & 0 & 0 & 0 \\ 0 & 0 & 0 & 0 & (1+\frac{\sigma_x}{\mathrm{i}\omega})/\rho_0 \\ 0 & 0 & 0 & 0 & 0 \\ 0 & 0 & \gamma p_0(1+\frac{\sigma_x}{\mathrm{i}\omega}) & 0 & 0 \end{bmatrix},$$

$$\mathbf{C}_{\text{pml}} = \begin{bmatrix} \mathrm{i}\omega + \sigma_D & \bar{\sigma}_x\rho_0\left(1+\frac{\sigma_r}{\mathrm{i}\omega}\right) & \frac{\rho_0}{r}\frac{\sigma_x}{\mathrm{i}\omega} & \rho_0\frac{\mathrm{i}m}{r}\left(1+\frac{\sigma_{x,r}}{\mathrm{i}\omega}\right) & 0 \\ 0 & \mathrm{i}\omega + \sigma_D & 0 & 0 & \bar{\sigma}_x\frac{1}{\rho_0}\left(1+\frac{\sigma_r}{\mathrm{i}\omega}\right) \\ 0 & 0 & \mathrm{i}\omega + \sigma_D & 0 & 0 \\ 0 & 0 & 0 & \mathrm{i}\omega + \sigma_D & \frac{1}{\rho_0}\frac{\mathrm{i}m}{r}\left(1+\frac{\sigma_{x,r}}{\mathrm{i}\omega}\right) \\ 0 & \bar{\sigma}_x\gamma p_0\left(1+\frac{\sigma_r}{\mathrm{i}\omega}\right) & \frac{\gamma p_0}{r}\left(1+\frac{\sigma_x}{\mathrm{i}\omega}\right) & \gamma p_0\frac{\mathrm{i}m}{r}\left(1+\frac{\sigma_{x,r}}{\mathrm{i}\omega}\right) & \mathrm{i}\omega + \sigma_D \end{bmatrix}, \tag{5}$$

where $\sigma_D = \sigma_{x,r} + \bar{\sigma}_x u_0(1+\sigma_r/\mathrm{i}\omega)$; $\sigma_{x,r} = \sigma_x + \sigma_r + \sigma_x\sigma_r/\mathrm{i}\omega$; $\bar{\sigma}_x = (\sigma_x/c_0)M_0/1 - M_0^2$; and $M_0 = u_0/c_0$. The damping constants σ_x and σ_r are of the same units as ω and are given by

$$\sigma_x = (1-M_0^2)\frac{c_0}{L_{\text{ref}}}\sigma_{x,\max}\left|\frac{x-x_i}{L_x}\right|^{\beta}, \quad \sigma_r = \frac{c_0}{L_{\text{ref}}}\sigma_{r,\max}\left|\frac{r-r_i}{L_r}\right|^{\beta}. \tag{6}$$

Here c_0 is the speed of sound in the PML, L_{ref} is a reference length, L_x and L_r are the widths of the PMLs in the x- and r-directions, respectively, and x_i and r_i are the locations of the interfaces between the PMLs and LEE domains in the x- and r-directions, respectively. The value of β is taken as 2, and $\sigma_{\max}\Delta x/L_{\text{ref}}$ is usually set to 2–4.

In order to excite the field with sources from the duct inlets, the PML equations are applied to the reflected wave components. Assuming the total acoustic field is composed of an incident field plus the reflected waves,

$\hat{\mathbf{q}} = \hat{\mathbf{q}}_{\text{in}} + \hat{\mathbf{q}}_{\text{re}}$, we can write

$$\mathbf{A}_{\text{pml}} \frac{\partial \hat{\mathbf{q}}}{\partial x} + \mathbf{B}_{\text{pml}} \frac{\partial \hat{\mathbf{q}}}{\partial r} + \mathbf{C}_{\text{pml}} \hat{\mathbf{q}} = \mathbf{A}_{\text{pml}} \frac{\partial \hat{\mathbf{q}}_{\text{in}}}{\partial x} + \mathbf{B}_{\text{pml}} \frac{\partial \hat{\mathbf{q}}_{\text{in}}}{\partial r} + \mathbf{C}_{\text{pml}} \hat{\mathbf{q}}_{\text{in}}, \tag{7}$$

where subscript 'in' refers to the incident field. The incident waves are constructed using cylindrical duct eigensolutions obtained from the solution of convected wave equation for pressure perturbation. The velocity perturbations are found by substituting the pressure solution into the LEE. This procedure gives

$$\hat{p}_{\text{in}} = \sum_n A^+_{mn} [J_m(k_{mn} r) + Q_{mn} Y_m(k_{mn} r)] \exp[\mathrm{i}(-k^+_{x,mn} x + m\theta)], \tag{8}$$

$$\hat{\rho}_{\text{in}} = \tilde{\rho} \exp(-\mathrm{i} k_{x,mn}) = \hat{p}_{\text{in}} / c_0^2, \tag{9}$$

$$\hat{u}_{\text{in}} = \tilde{u} \exp(-\mathrm{i} k_{x,mn}) = \frac{k^+_{x,mn} \hat{p}}{\rho_0(\omega - u_0 k^+_{x,mn})}, \tag{10}$$

$$\hat{v}_{\text{in}} = \tilde{v} \exp(-\mathrm{i} k_{x,mn}) = -\frac{\partial \hat{p}/\partial r}{\mathrm{i}\rho_0(\omega - u_0 k^+_{x,mn})}, \tag{11}$$

$$\hat{w}_{\text{in}} = \tilde{w} \exp(-\mathrm{i} k_{x,mn}) = -\frac{\partial \hat{p}/\partial \theta}{\mathrm{i}\rho_0 r(\omega - u_0 k^+_{x,mn})}, \tag{12}$$

where $k^+_{x,mn}/k = [-M + \sqrt{1 - (1 - M^2)(k_{mn}/k)^2}]/(1 - M^2)$ with $k = \omega/c_0$; A_{mn} is a constant; J_m and Y_m are the mth-order Bessel functions of the first and second kind, respectively; $Q_{mn} = Y'_m(\sigma k_{mn} r_o)/J'_m(\sigma k_{mn} r_o)$, and $\sigma = r_i/r_o$ (ratio of inner radius to outer radius), and n is the radial mode order.

2.2.2. Wall boundary conditions

Consistent with the solution of the LEE, slip wall conditions are applied at a hard wall, although the background flow may totally be viscous. When a liner element exists on a wall, the frequency-dependent boundary condition of Myers [1] is employed. Thus, at a hard-wall the normal velocity perturbation is set to zero, while the tangential contravariant velocity perturbations are extrapolated from the interior solution. The density perturbation is also extrapolated from the interior points. Then, the pressure perturbation is found from the normal momentum balance as described in Ref. [18]. The resulting wall boundary condition equations are written in the same vector form as that of the LEE or PML equations (i.e., Eq. (3)) so that the same schemes can be applied in a compact form with corresponding differencing and interpolation weights.

2.3. Far-field prediction

Far-field sound pressure levels (SPL) are computed employing a Kirchhoff surface integration. While in no-flow cases a closed Kirchhoff surface is preferred, an open Kirchhoff surface is more suitable when a jet flow exists. The Kirchhoff integration is based on the moving surface Kirchhoff formula of Farassat and Myers [19].

For the present type of problems, the flow velocity is $\mathbf{M}_\infty$ and in the $+x$-direction away from the source (engine), where the Kirchhoff surface should theoretically be located. Hence, the flow is sensed by a Kirchhoff surface fixed relative to the engine as moving in the negative x-direction. Assuming we have this situation, the far-field sound is extrapolated to the observer location $\mathbf{x}_{\text{o}}$ by

$$4\pi \hat{p}(\mathbf{x}_{\text{o}}, \omega) = \int\int_S \left[\frac{E_1}{R(1 - M_R)} + \frac{\hat{p} E_2}{R^2 (1 - M_R)} \right] \exp(-\mathrm{i} k R)\, \mathrm{d}S, \tag{13}$$

where

$$E_1 = -\mathbf{n} \cdot \nabla \hat{p} + (\mathbf{M}_\infty \cdot \mathbf{n})(\mathbf{M}_\infty \cdot \nabla \hat{p}) + \left[\frac{\cos\phi + \mathbf{M}_\infty \cdot \mathbf{n}}{c_\infty (1 - M_R)} + \frac{\mathbf{M}_\infty \cdot \mathbf{n}}{c_\infty} \right] \mathrm{i}\omega \hat{p}, \tag{14}$$

$$E_2 = \frac{1 - M_\infty^2}{(1 - M_R)^2} (\cos\phi + \mathbf{M}_\infty \cdot \mathbf{n}) \tag{15}$$

and $k=\omega/c_\infty$, $M_\infty=|\mathbf{M}_\infty|$, $R=|\mathbf{R}|$, $\mathbf{R}$ is the radiation distance vector from the surface to the observer along which the waves propagate, $M_R=-\mathbf{M}_\infty\cdot\mathbf{R}/R$, and with ϕ being the angle between the surface outward normal $\mathbf{n}$ and the radiation direction indicated by the vector $\mathbf{R}$. The Cartesian components of the radiation vector $\mathbf{R}$ may be given as

$$R_x=\Delta x_{\mathrm{os}}-M_\infty\left[\Delta x_{\mathrm{os}}^2+(1-M_\infty^2)(\Delta y_{\mathrm{os}}^2+\Delta z_{\mathrm{os}}^2)\right]^{1/2}, \tag{16}$$

$$R_y=\Delta y_{\mathrm{os}}, \tag{17}$$

$$R_z=\Delta z_{\mathrm{os}}, \tag{18}$$

where $\Delta\mathbf{x}_{\mathrm{os}}=\mathbf{x}_{\mathrm{o}}-\mathbf{x}_{\mathrm{s}}$ is the physical distance vector from the Kirchhoff surface (s) to the observer (o).

2.4. Algorithm development

One of the most important aspects of a computational aeroacoustics scheme is its approximation to the dispersion relation of the governing equations. The numerical scheme must preserve the physical dispersion relation for a wide range of wavenumbers. This can be shown to be dependent strongly on the discretization of the derivatives and the grid resolution employed. It has been well established that high-order schemes have better dispersion properties [20]. However, such algorithms usually have wide stencils which may be difficult to deal with computationally. This is especially true in the present approach, as it deals with direct inversion of large linear systems of equations. Wide stencils result in large bandwidth sparse coefficient matrices, and very quick fill-ins occur during their direct inversion using a Gaussian elimination or LU type factorization. This causes inefficiencies and large memory requirements, even for the state-of-the-art direct solvers, such as MUMPS [21] and SuperLU [22]. Therefore, to these respects an evaluation of various discretization schemes has been needed in the present work. Three different algorithms have been implemented. These are the (i) standard 4th-order finite difference, (ii) dispersion relation preserving (DRP) scheme of Tam and Webb [20], (iii) linear B-spline Galerkin method [23]. The interior stencils employed by these schemes are shown in Fig. 2.

All the equations, including the boundary conditions, are transformed into a body fitted coordinate system through the mappings $x=x(\xi,\eta)$ and $r=r(\xi,\eta)$. The transformed equations may be written in the form

$$\bar{\mathbf{A}}\frac{\partial\hat{\mathbf{q}}}{\partial\xi}+\bar{\mathbf{B}}\frac{\partial\hat{\mathbf{q}}}{\partial\eta}+\bar{\mathbf{C}}\hat{\mathbf{q}}=\bar{\mathbf{r}}. \tag{19}$$

All of the schemes applied to the above equation may be written in the following difference operator form:

$$\sum_{v=1}^{5}\sum_{r=-M_r}^{N_r}\sum_{s=-M_s}^{N_s}\{\phi_s^{i,j}\,\bar{A}_{e,v}^{i,j+s}\,a_r^{i,j}+\psi_r^{i,j}\,\bar{B}_{e,v}^{i+r,j}\,b_s^{i,j}+\phi_s^{i,j}\,\psi_r^{i,j}\,\bar{C}_{e,v}^{i+r,j+s}\}\,\hat{q}_v^{i+r,j+s}=\sum_{r=-M_r}^{N_r}\sum_{-M_s}^{N_s}\phi_s^{i,j}\,\psi_r^{i,j}\,\bar{r}_e^{i+r,j+s}, \tag{20}$$

where a superscript pair (e.g., i,j) refers to a grid point index (address), $\bar{A}_{e,v}=\bar{\mathbf{A}}$, $\bar{B}_{e,v}=\bar{\mathbf{B}}$, and $\bar{C}_{e,v}=\bar{\mathbf{C}}$ with e indicating the equation index ($e=1,2,3,4$, and 5 correspond to the continuity, axial momentum, radial momentum, azimuthal momentum, and energy equations, respectively), v indicating the dependent variable index ($q_{v=1,2,3,4,5}$ refers to the density perturbation, axial velocity perturbation, radial velocity perturbation, azimuthal velocity perturbation, and pressure perturbation, respectively). The interpolation weights are denoted as ϕ and ψ, and the finite difference weights are denoted as a and b. These weights are assigned according to the scheme and the grid point.

2.4.1. Dispersion characteristics of the schemes

All of the three schemes mentioned above have different wave propagation characteristics. Consider that we have the following 2-D advection equation for a single dependent variable $\hat{u}$ in the frequency domain,

$$\mathrm{i}\omega\hat{u}+c_x\frac{\partial\hat{u}}{\partial x}+c_y\frac{\partial\hat{u}}{\partial y}=0, \tag{21}$$

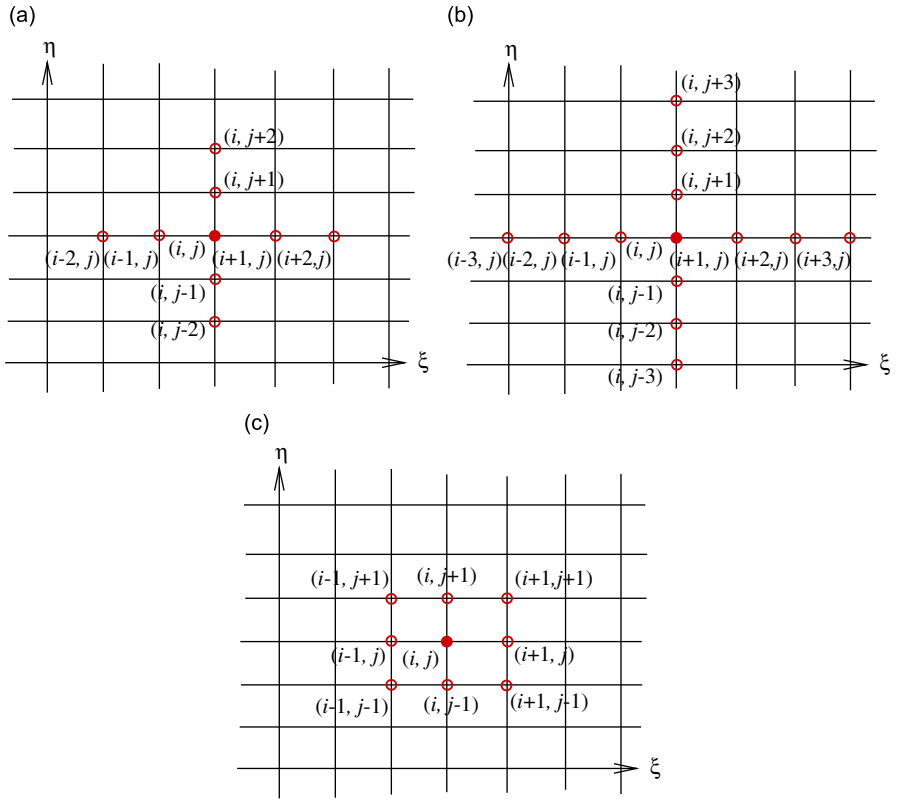

Fig. 2. The interior stencils used by (a) the standard 4th-order scheme, (b) DRP scheme, and (c) the B-spline Galerkin scheme.

where $c_x = c\cos\theta$ and $c_y = c\sin\theta$ are propagation speeds in the x- and y-directions, respectively. Spatial Fourier transform of the above equation leads to the following exact dispersion relation:

$$\mathrm{i}\omega - \mathrm{i}c_x k_x - \mathrm{i}c_y k_y = 0 \quad \text{with } c^2 = c_x^2 + c_y^2 = \omega^2/k^2 \text{ and } k^2 = k_x^2 + k_y^2. \tag{22}$$

Here c is the exact phase speed for the above advection equation.

Spatial Fourier transform of the discrete form of Eq. (21) on a uniform mesh with $\Delta x = \Delta y$ leads to the following discrete dispersion relation:

$$\sum_{r=-M_r}^{N_r}\sum_{s=-M_s}^{N_s}\left\{\mathrm{i}\omega\phi_s^{i,j}\psi_r^{i,j}\exp[-\mathrm{i}(rk_x+sk_y)\Delta x] + \frac{\mathrm{i}c}{\Delta x}(\cos\theta\phi_s^{i,j}a_r^{i,j} + \sin\theta\psi_r^{i,j}b_s^{i,j})\exp[-\mathrm{i}(rk_x+sk_y)\Delta x]\right\} = 0, \tag{23}$$

where from the exact dispersion relation $k_x = k\cos\theta$ and $k_y = k\sin\theta$. If this numerical dispersion relation is written in the form

$$\mathrm{i}\omega - \mathrm{i}kc^* = 0. \tag{24}$$

By comparison the normalized numerical speed of propagation $a^* = c^*/c$ is found to be in the form

$$a^* = -\frac{1}{k\Delta x}\cdot\frac{\sum_{r=-M_r}^{N_r}\sum_{s=-M_s}^{N_s}(\cos\theta\phi_s^{i,j}a_r^{i,j} + \sin\theta\psi_r^{i,j}b_s^{i,j})\exp[-\mathrm{i}(rk_x+sk_y)\Delta x]}{\sum_{r=-M_r}^{N_r}\sum_{s=-M_s}^{N_s}\phi_s^{i,j}\psi_r^{i,j}\exp[-\mathrm{i}(rk_x+sk_y)\Delta x]}. \tag{25}$$

In this relation $k\Delta x$ may be written for a given number of grid points per wavelength (NPPW) as $k\Delta x = 2\pi/\mathrm{NPPW}$, and following this relation $k_x\Delta x = 2\pi\cos\theta/\mathrm{NPPW}$ and $k_y\Delta x = 2\pi\sin\theta/\mathrm{NPPW}$.

Figs. 3–5 show polar plots of the normalized numerical wave speed for the standard 4th-order central difference (FD4), dispersion relation preserving (DRP) scheme, and linear B-spline Galerkin method with 6, 10, 14 grid points per wavelength (NPPW), respectively. It is evident, especially from the close-up views in

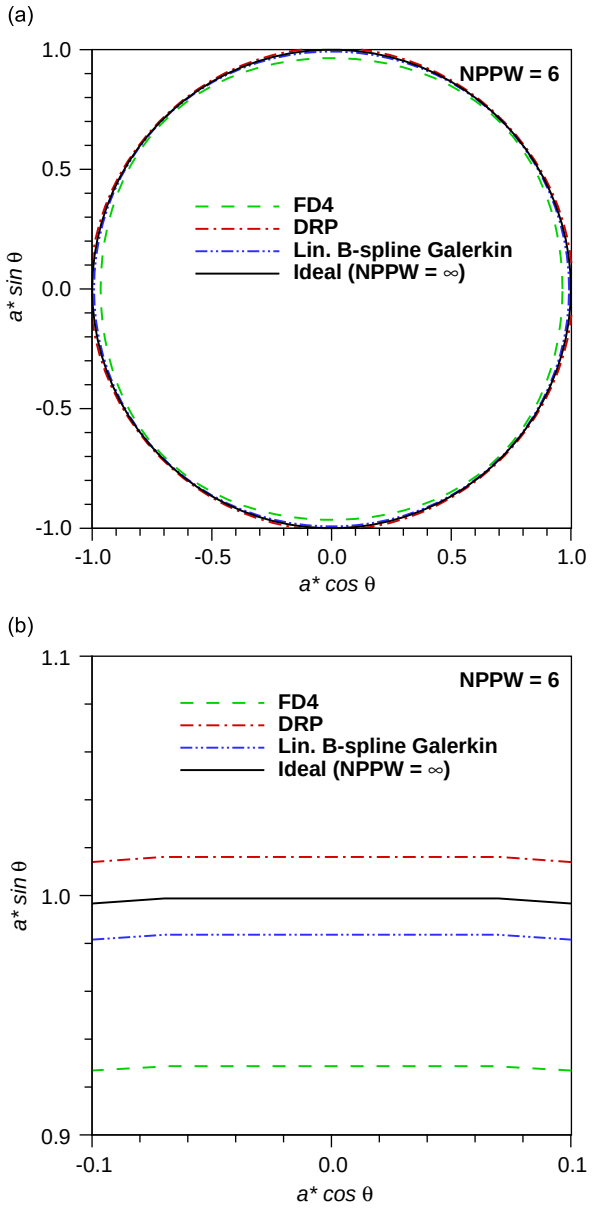

Fig. 3. Polar plot of the numerical phase velocity, NPPW $= \lambda/\Delta x = 6$. (a) Full view, (b) close-up view.

these plots, that for all the resolutions shown, the linear B-spline Galerkin method looks superior over the other two schemes. While the FD4 scheme looks reasonable for NPPW = 14, it starts behaving poorly toward NPPW = 10 and under. While the numerical phase speed captured by the B-spline Galerkin scheme for NPPW = 6 is over 98% of the physical wave speed, this ratio is close to 102% by the DRP scheme, and to 93% by the FD4 scheme.

It is clear that among the three the ideal scheme is either the DRP or a Galerkin type algorithm. In terms of memory requirements during the direct solution phase, the B-spline Galerkin algorithm seems certainly more advantageous over the DRP scheme, because the former method requires a more compact stencil (Fig. 2), and hence a smaller bandwidth. However, there are some difficulties with the B-spline Galerkin method at or near boundaries. Suitable B-splines must be defined. Usually the ones defined at or near boundaries with simple differences destroy the high resolution nature. Numerical experimentation in the present work showed that

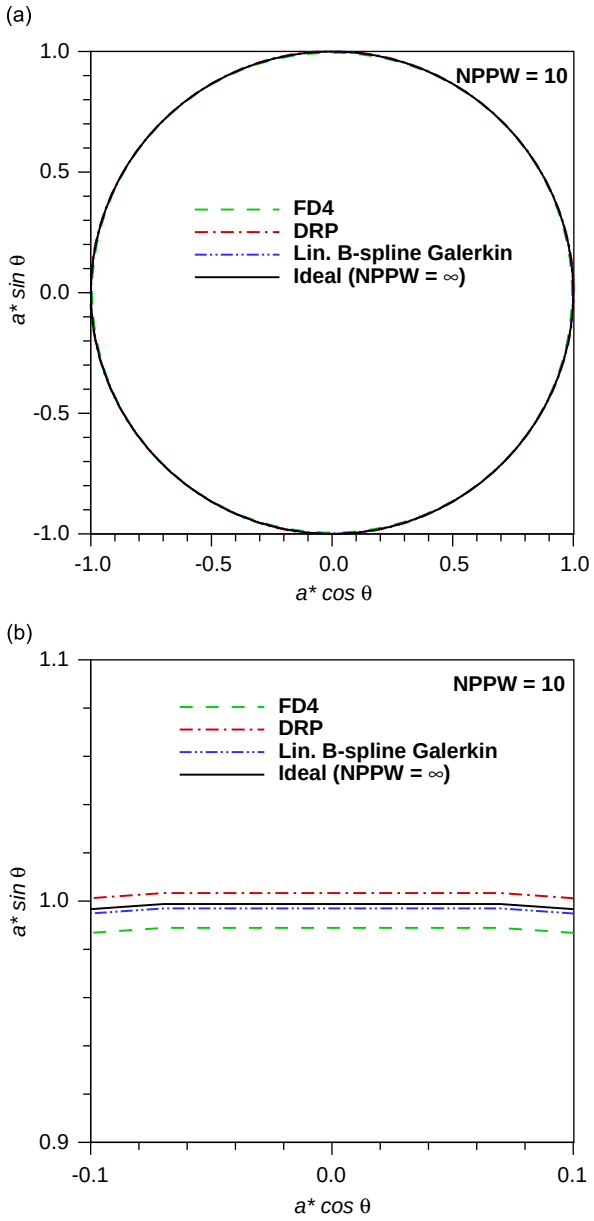

Fig. 4. Polar plot of the numerical phase velocity, NPPW $= \lambda/\Delta x = 10$. (a) Full view, (b) close-up view.

with the linear B-spline Galerkin discretization at the interior points and some low-order finite difference procedure at the boundaries, grid to grid oscillations arise, and these are more pronounced near sharp edges. Because of its lower bandwidth requirement and better behavior near the boundaries the standard 4th-order scheme appeared more feasible for most situations than the DRP and B-spline Galerkin schemes, provided that sufficient grid resolution is used.

2.4.2. *Linear system of equations and its solution*

The discretization of the governing equations and the boundary conditions results in a linear system of equations with complex coefficients and right-hand sides. The whole assembled system is written as

$$\hat{\mathbf{A}}_g \hat{\mathbf{q}}_g = \hat{\mathbf{r}}_g, \tag{26}$$

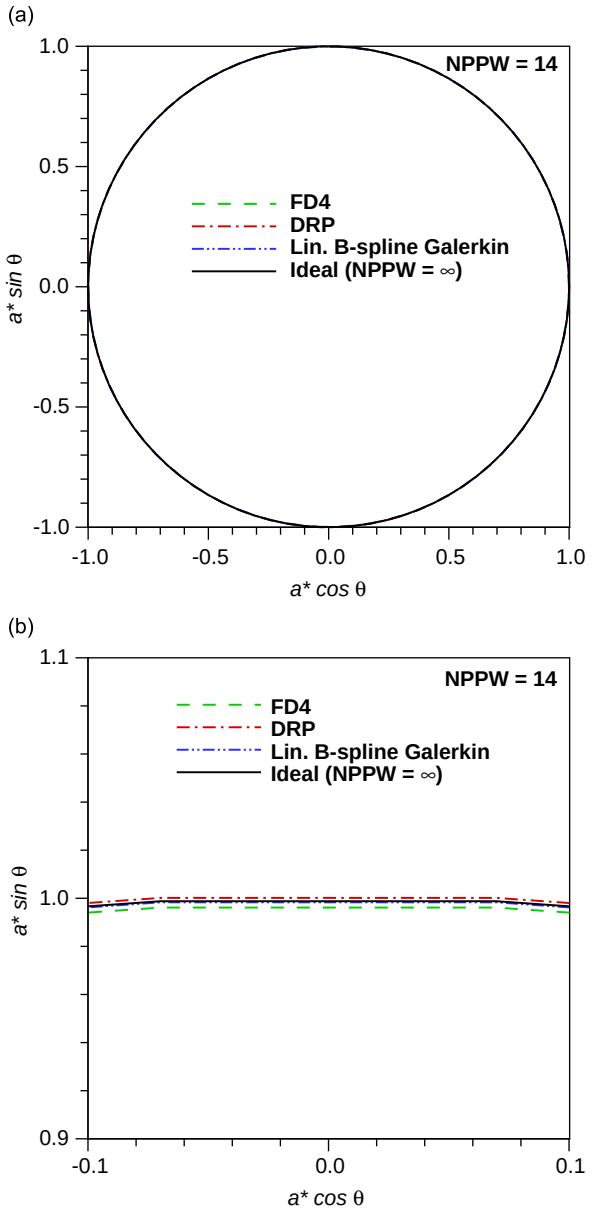

Fig. 5. Polar plot of the numerical phase velocity, NPPW $= \lambda/\Delta x = 14$. (a) Full view, (b) close-up view.

where $\hat{\mathbf{A}}_g$ represents the global coefficient matrix, $\hat{\mathbf{q}}_g$ is the global solution vector, and $\hat{\mathbf{r}}_g$ is the global right-hand side vector. The coefficient matrix $\hat{\mathbf{A}}_g$ is quite sparse. In Fig. 6 the non-zero entry locations of a coefficient matrix that resulted on a small structured mesh using the standard, 4th-order differencing is shown. The entries of the matrix fall around five bands which are separated from each other as a function of the number of grid points. The direct inversion of such a matrix with all entries is prohibitive for most problems. Therefore, for an efficient direct solution, a parallel, sparse solver is employed. Provided sufficient memory on the computing platform, the multifrontal massively parallel sparse direct solver MUMPS [21] has been found quite effective to solve this kind of equation systems. This is a distributed memory sparse solver based on an LU or LDL^T factorization of the matrix using a multifrontal technique [24,25].

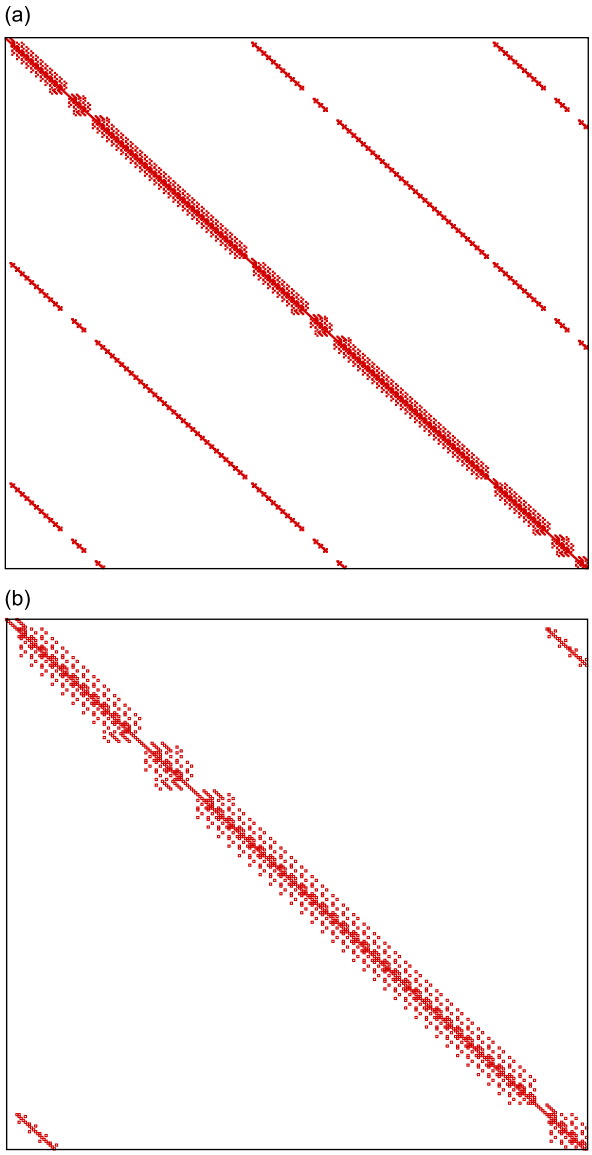

Fig. 6. Sparse nature of the coefficient matrix as obtained using the FD4 scheme—non-zero entry locations shown. (a) Full view, (b) close-up view of the diagonal band.

3. Verification of the solver

3.1. Wave propagation in infinite circular duct with flow

The developed code is tested first for propagation of spinning modes through an infinite circular duct with flow. The radius of the duct is chosen as 1.212 m, without a centerbody. Although the considered problem is for an infinite duct, the numerical solution is carried out in a finite size domain with the PML equations solved in two narrow layers just inside the duct inlet and outlet, respectively. Waves are introduced from both the inlet and outlet PMLs. By setting up the problem this way, we actually test both accuracy of the developed schemes and the ability of the PML equations for introducing spinning modes into the computational domain and at the same time absorbing the outgoing waves. This is particularly important as there will be reflections from the edges of acoustic treatment panels (liners) and duct sections where local impedance variation exists,

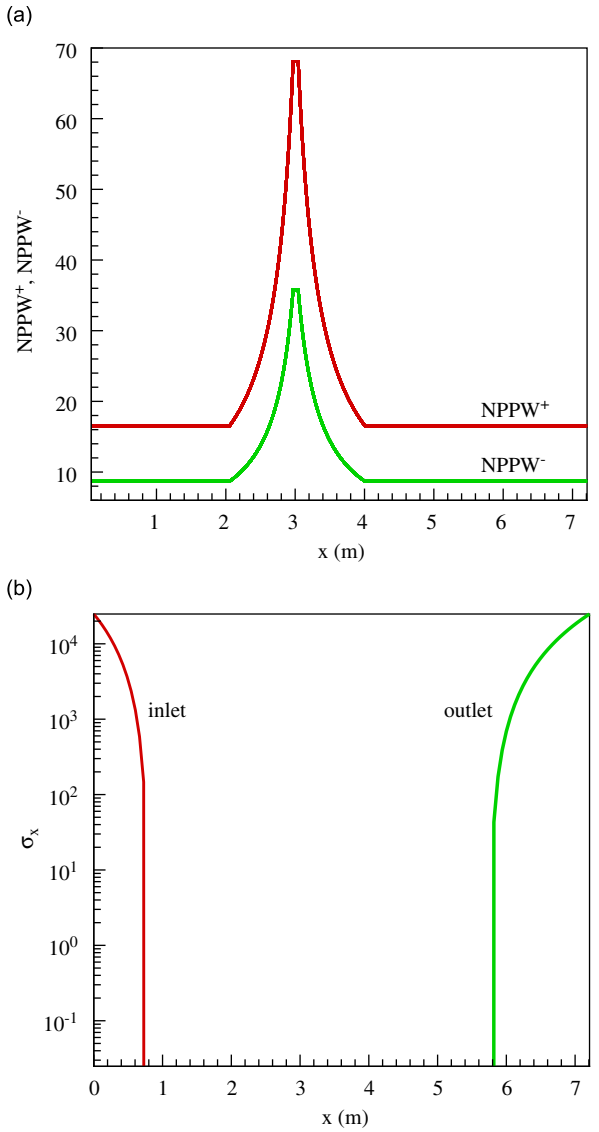

Fig. 7. Variation of the grid resolution and damping factor for mode (19,1) calculations at $M_c = 0.459$, $f = 866$ Hz. (a) Grid resolution, (b) damping factor σ_x.

such as the exit section of a finite duct. On the computational mesh used for this test problem grid points are clustered near the duct wall and about an axial section along the duct. Such clusterings would normally be needed in actual engine problems, for example near the nozzle lip.

The problem is solved at two different operating conditions. In the first the flow Mach number and the frequency are taken as 0.459 and 866 Hz, respectively. The highest azimuthal mode order that is cut on at these conditions is $m = 19$. The first radial mode [the (0,1) mode is the plane wave mode in this paper] is considered in the simulations. The mesh used for this mode has the resolutions shown in Fig. 7 for the downstream and upstream propagating (19,1) modes. The damping factors used in the PMLs are also plotted on the right of the same figure. It is clear from the figure that there are fewer than 10 points per wavelength for the upstream propagating waves for a significant part of the duct. There happened to be nearly 35 grid points per wavelength at about $x = 3$ m because of clustering applied there. For the downstream propagating waves these resolutions are a little bit higher than 18 points in the unclustered part, and about 68 points per wavelength in the clustered region. The PMLs are taken as about 0.8 and 1.2 m thick in the inlet and outlet regions,

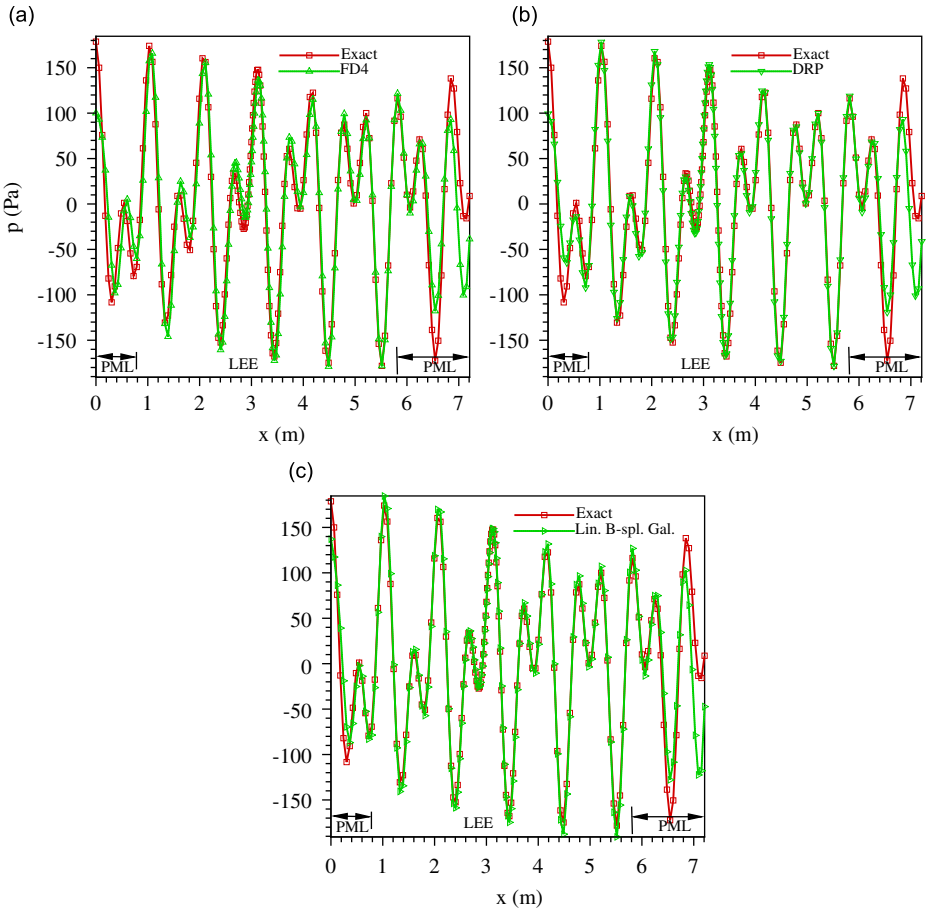

Fig. 8. Comparison of the computed wall pressure (real part) with exact solution for the (19,1) mode at $M_c = 0.459$, $f = 866$ Hz. (a) Standard 4th-order solution versus exact, (b) DRP solution versus exact, (c) B-spline Galerkin solution versus exact.

respectively. The damping factors are varied from zero at the interface between the interior LEE region and PML to about 36 000 by the inlet and outlet. Note the logarithmic scale for the damping factor in Fig. 7. The (19,1) modes are introduced from both ends of the duct. The results are obtained using the standard 4th-order difference scheme, DRP scheme, and the linear B-spline Galerkin discretization.

Comparisons of the computed wall pressure with the exact solution are provided in Fig. 8. It is clear that except in the PMLs at the inlet and outlet where damping exists, the agreement between the numerical solutions and exact solution is excellent, showing the effectiveness of the PML equations for both absorbing the outgoing waves and introducing the desired waves. Also the developed schemes capture the important characteristics of the spinning waves quite accurately.

The same case is also solved on a uniform mesh with 16 grid points per length for the downstream propagating waves. No upstream propagating waves are introduced. The domain length is set to about 6 m, in which 100 grid points are distributed. A total of 30 grid points are distributed in the radial direction. The standard 4th-order finite difference scheme is employed for the solution. The computed fields of acoustic pressure and radial velocity are compared to the exact solution in Fig. 9. The agreement is excellent.

The second operating condition at which solutions are obtained involves a much faster flow. The flow Mach number is taken as 0.855, and the wave frequency is taken as 1580 Hz. A uniform mesh with 850×40 grid points is used for the calculations, corresponding to about 10 points per length for the downstream propagating waves. Again the standard 4th-order scheme is used. The calculated acoustic field is shown in comparison with the exact solution near the inlet and outlet of the duct in Fig. 10. Due to insufficient grid resolution some phase error build-up is observed as the waves approach the outlet of the duct.

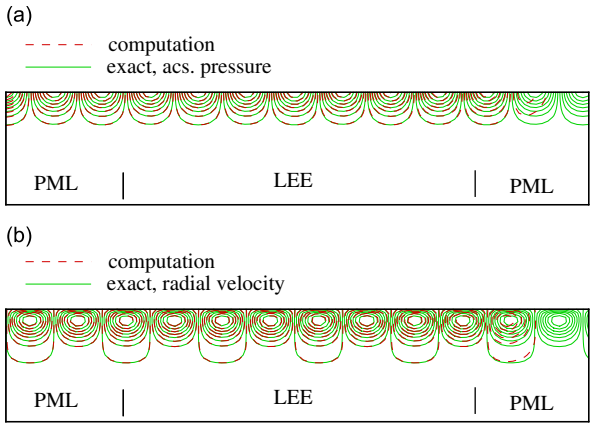

Fig. 9. Comparison of the computed acoustic field (real part) of the (19,1) mode with exact solution: (a) Acoustic pressure, (b) radial velocity. $M_c = 0.459$, $f = 866$ Hz.

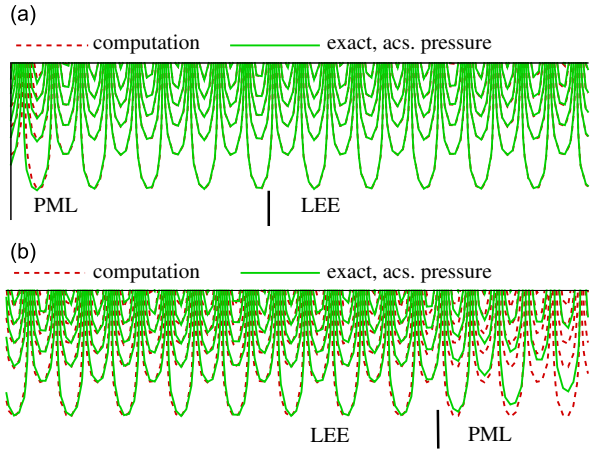

Fig. 10. Comparison of the computed acoustic pressure (real part) of the (63,1) mode with exact solution: (a) Near inlet, (b) near outlet. $M_c = 0.855$, $f = 1580$ Hz.

We can conclude from the study in this section that the developed code accurately calculates the important features of spinning waves in the frequency domain, provided sufficient grid resolution exists in required regions. The PML implementation works excellently for both upstream and downstream propagating waves.

3.2. Radiation from semi-infinite ducts

In this section we test the developed code against two types of semi-infinite ducts. These are (1) a semi-infinite circular duct (Duct 1) (2) a semi-infinite annular duct with an infinite centerbody (Duct 2). Both ducts have an inner radius of 0.947 m and an outer radius of 1.212 m. These duct configurations are shown in Fig. 11. Computations are done using the 4th-order finite difference algorithm. In all the cases computed in this section, the modes are introduced into the ducts via the PML equations with a unit intensity definition of Ref. [26].

3.2.1. Radiation from Duct 1

Two different operating conditions are considered for this duct configuration. In the first the frequency is set to 956 Hz, while no flow condition is specified inside and outside the duct. The corresponding dimensionless frequency is $kr_o = 21.4$. The spinning $m = 19$ and 10 modes are computed. Three radial modes are cut on for

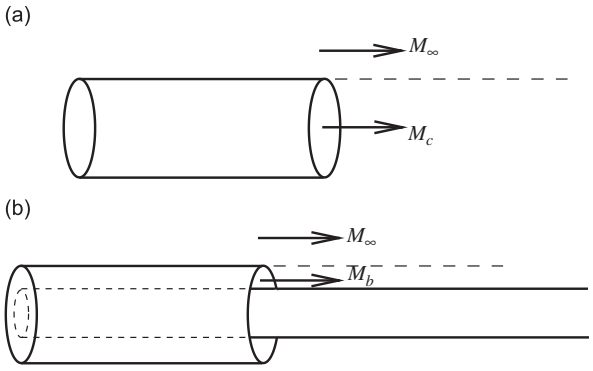

Fig. 11. (a) Duct configuration 1 and (b) duct configuration 2. $r_i = 0.947\,\text{m}$, $r_o = 1.212\,\text{m}$.

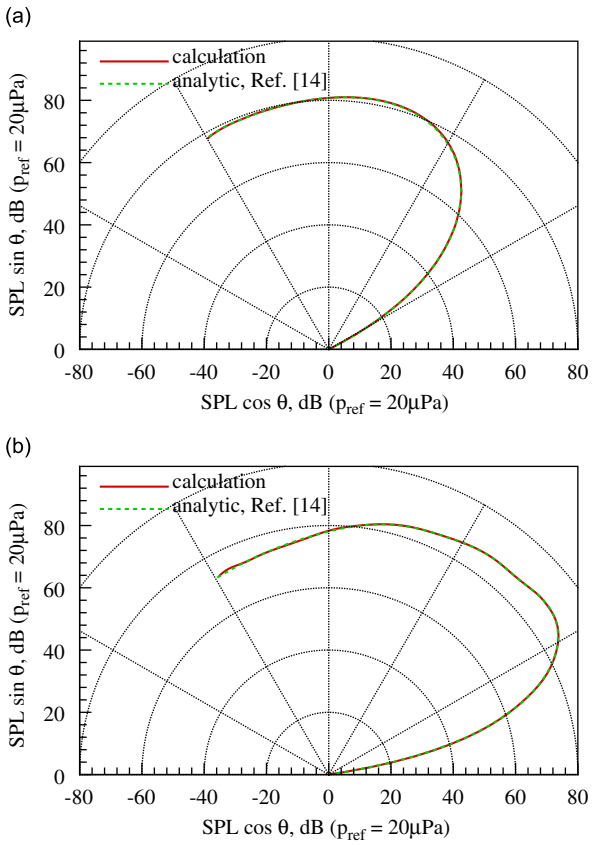

Fig. 12. Comparison of computed far-field sound pressure levels on a 46-m arc from the Duct 1 termination and extended Munt's model solutions of Demir and Rienstra [14] at $f = 956\,\text{Hz}$, $M_\infty = 0$, $M_c = 0$, $kr_o = 21.4$. (a) (19,1) mode and (b) $m = 10$ mode with all cut-on radial modes.

$m = 10$, and only one radial mode propagates for $m = 19$ which is the highest azimuthal cut-on mode at these conditions. In Fig. 12, the far-field SPL obtained along a 46-m arc from the duct termination using a closed Kirchhoff surface are shown together with the extended Munt's model solutions of Demir and Rienstra [14]. The far-field SPL plot for the $m = 10$ mode contains incoherent contributions of all the cut-on radial modes. That is, SPL for $m = 10$ was computed using $p^2_{m,\text{rms}} = (1/n_{\max})\sum_{n=1}^{n_{\max}} p^2_{\text{mn,rms}}$. It is evident from the figures that the present numerical solutions and the analytical solutions agree quite well.

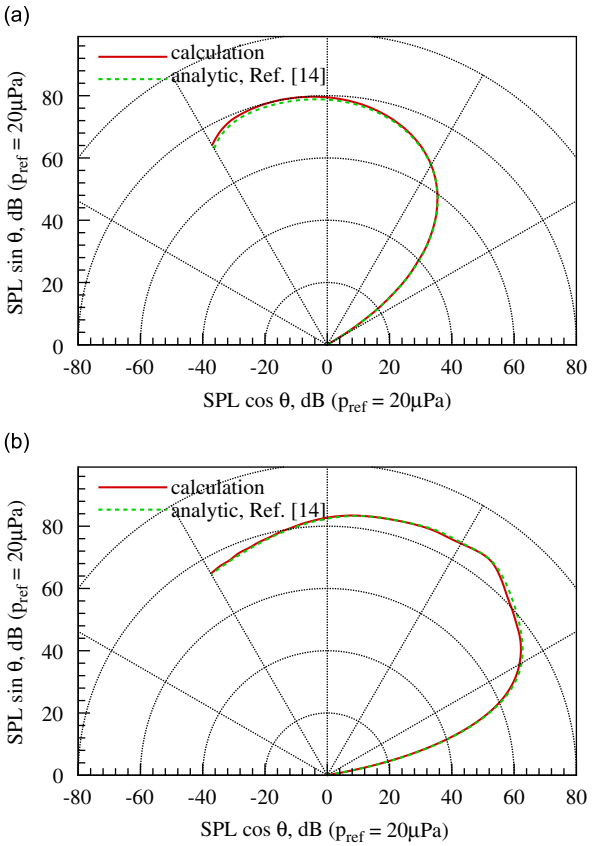

Fig. 13. Comparison of computed far-field sound pressure levels on a 46-m arc from the Duct 1 termination and extended Munt's model solutions of Demir and Rienstra [14] at $f = 866$ Hz, $M_\infty = 0.219$, $M_b = 0.447$, $kr_o = 19$. (a) (19,1) mode and (b) $m = 10$ mode with all cut-on radial modes.

We consider a plug flow situation for the second operating condition for duct configuration 1. We simply set the flow speeds through the duct and exterior to it to uniform Mach number values of $M_c = 0.447$ and $M_\infty = 0.219$, respectively. This implies an infinitely thin shear layer exists between the flow issuing from the duct and the external stream. However, in the present implementation no grid points lie along this separation line between the two streams, as the solver is based on cell-centered finite differences. Again the spinning mode orders of $m = 19$ and 10 are solved but at a frequency of 866 Hz. At the considered flow condition through the duct, one radial mode is cut on for $m = 19$, and two radial modes are cut on for $m = 10$. The contributions of both radial modes are included in the far-field results for the latter azimuthal mode, as in the previous case. The computed far-field SPLs are compared with the analytical solutions of again Ref. [14], in Fig. 13. Despite the open Kirchhoff surface used for the far-field computations, the peak values of the main lobes as well as their radiation directions were captured quite accurately for both azimuthal modes.

3.2.2. *Radiation from Duct 2*

For this duct configuration we consider two different operating conditions. In the first, the flow Mach numbers for the flow through the annular part of the duct and outside stream are set to uniform values of $M_b = 0.447$ and $M_\infty = 0.219$, respectively. Again between the duct flow and external stream an infinitely thin shear layer is assumed to exist. The frequency for the duct modes is taken as 866 Hz, corresponding to a dimensionless frequency of $kr_o = 19$. The highest spinning mode order at these conditions is (19,1) mode. Along with this mode, results are also obtained for the $m = 10$ mode. For the latter two radial modes

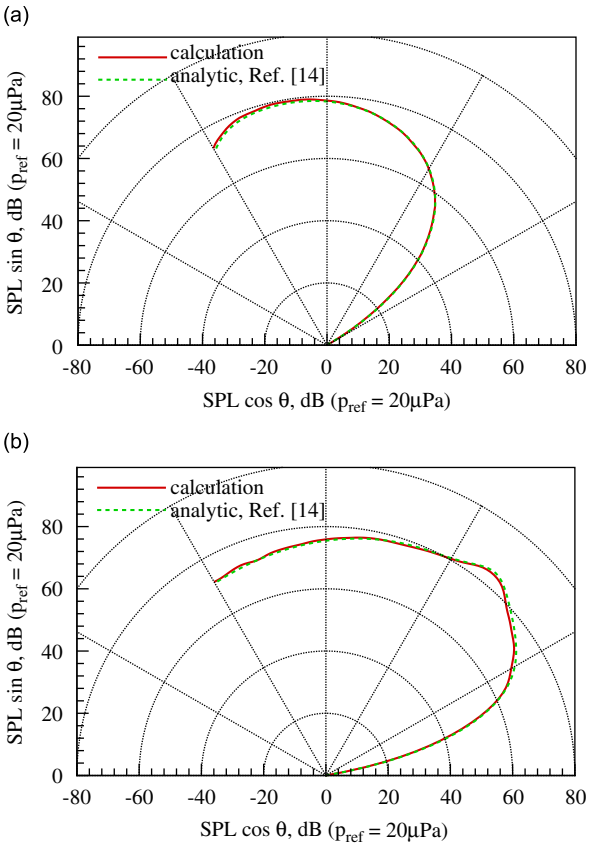

Fig. 14. Comparison of computed far-field sound pressure levels on a 46-m arc from the termination of Duct 2 passage and extended Munt's model solutions of Demir and Rienstra [14] at $f = 866$ Hz, $M_\infty = 0.219$, $M_b = 0.447$, $kr_o = 19$. (a) (19,1) mode and (b) $m = 10$ mode with all cut-on radial modes.

propagate, and their contributions are summed incoherently. Fig. 14 compares the computed far-field SPLs with again the analytical solutions of Ref. [14]. The agreement between the numerical predictions and analytical solutions is very good.

The second operating condition considers higher duct and external stream velocities and a higher frequency. The duct passage speed is increased to $M_b = 0.737$ while the external flow speed is increased to $M_\infty = 0.269$. The considered frequency is 1430 Hz. These conditions correspond to a dimensionless frequency of $kr_o = 31.2$. At these conditions the highest azimuthal mode that is cut on is the (43,1) mode. The other two modes solved in this test are the (23,1) and (0,1) modes. The computed near-field and far-field solutions are shown in Figs. 15–17, respectively. In these figures the calculated far-field results are also compared with the analytical solutions of Ref. [14]. It is clear from Fig. 15 that the radiated energy for the (43,1) mode is quite small. The far-field numerical and analytical results agree reasonably well for this mode. As seen in Fig. 16 the numerical and analytical solutions for the (23,1) mode agree quite well, in terms of the peak radiation direction as well as peak SPL. It is demonstrated in Fig. 17 the peak radiation directions and SPLs for the plane wave mode (0,1) were also captured quite accurately. However, the relatively poor agreement at lower angles for this mode is due to the limited size of the open Kirchhoff surface used.

3.2.3. Radiation from Duct 2 with lined centerbody

In this section we present example computations with a lined surface. In this case, we consider the Duct 2 geometry with its centerbody lined beyond the duct passage termination with a non-dimensional impedance value of $Z/\rho_b c_b = 2 - \mathrm{i}$. The operating conditions are the same as those of the first set Duct 2 computations

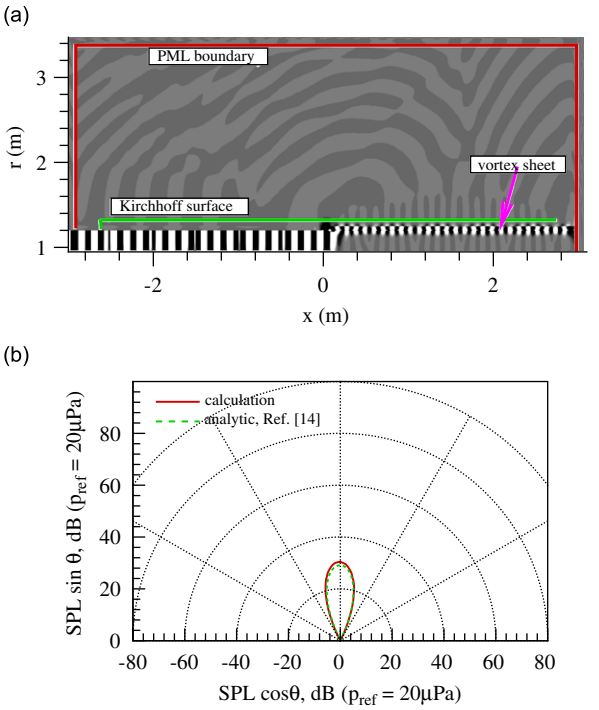

Fig. 15. (a) Acoustic pressure contours of the (43,1) mode (contour levels are from −2 to +2 Pa) and (b) comparison of computed far-field sound pressure levels on a 46-m arc from the termination of Duct 2 passage and extended Munt's model solution of Demir and Rienstra [14] at $f = 1430$ Hz, $M_\infty = 0.269$, $M_b = 0.737$, $kr_o = 31.2$.

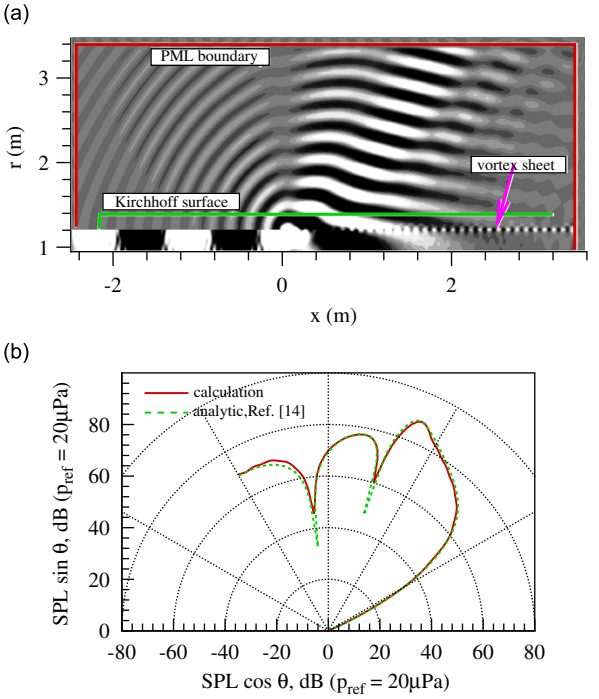

Fig. 16. (a) Acoustic pressure contours of the (23,1) mode (contour levels are from −5 to +5 Pa) and (b) comparison of computed far-field sound pressure levels on a 46-m arc from the termination of Duct 2 passage and extended Munt's model solution of Demir and Rienstra [14] at $f = 1430$ Hz, $M_\infty = 0.269$, $M_b = 0.737$, $kr_o = 31.2$.

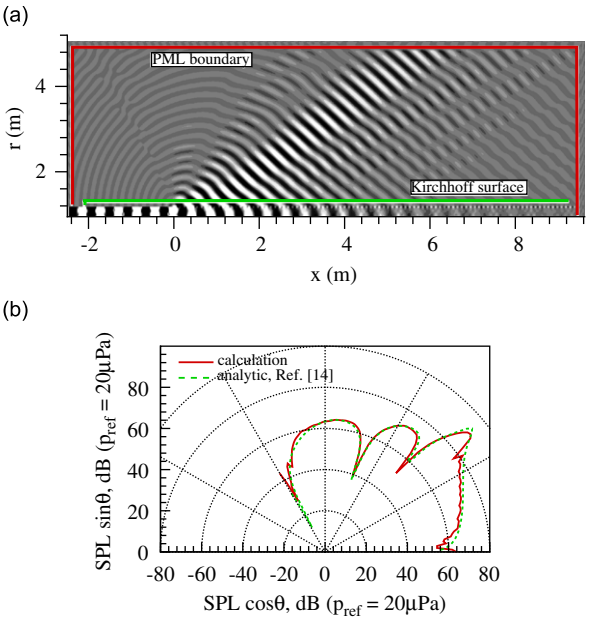

Fig. 17. (a) Acoustic pressure contours of the (0,1) mode (contour levels are from −5 to +5 Pa) and (b) comparison of computed far-field sound pressure levels on a 46-m arc from the termination of Duct 2 passage and extended Munt's model solution of Demir and Rienstra [14] at $f = 1430$ Hz, $M_\infty = 0.269$, $M_b = 0.737$, $kr_o = 31.2$.

presented above. The far-field results are obtained for the (19,1) and (10,1) modes, respectively. The computed results are compared with analytical solutions of Demir and Rienstra [14] in Fig. 18. The comparisons look as good as the hard-wall solutions presented in the previous two sections, showing the lined wall treatment capability of the present LEE solver.

3.3. *Radiation from realistic geometries and comparison with experiment*

In this section, the developed code is validated against the measured far-field acoustic data for two different engine exhaust cowls. These nozzles have been tested within the European Framework Programme 6 project TURNEX (Turbomachinery Noise Radiation through the Engine Exhaust) at QinetiQ, UK. One of these engines has a short exhaust cowl, and the other one has a long exhaust cowl, as shown in Figs. 19 and 20, respectively. The measurement and data post-processing procedures are described in detail in Arnold et al. [27] and Tapken et al. [28], respectively. No measurements for the mean flowfield are made, but the upstream (inlet) flow conditions for the core and bypass ducts are measured and provided. As the background flows at these conditions, the present study uses the Reynolds-averaged Navier–Stokes (RANS) solutions obtained through the commercial computational fluid dynamics (CFD) software Fluent [29] with the $k-\varepsilon$ turbulence model.

Calculations are done at the static approach condition for the short cowl and at the static cutback condition for the long cowl. To capture the effects of turbulence on the mean flow, the CFD meshes are generated with sufficient resolution near the walls and across the expected shear layer regions. The computed Mach number contours corresponding to the mean flowfields of the two cases are shown in Figs. 19 and 20, respectively. It is evident from the Mach contours that the flow accelerates by the nozzle exits, reaching about 0.45 for the short cowl, and about 0.68 for the long cowl. The development of the shear layers from the cowl trailing edges are also quite evident. The acoustic modes propagating through the bypass ducts radiate to the far-field through these layers.

Acoustic computations are done for a bypass spinning mode order of $m = 10$ at $f = 8504$ Hz for the short cowl, and for a bypass spinning mode order of $m = 9$ at $f = 5743$ Hz for the long cowl. The former azimuthal

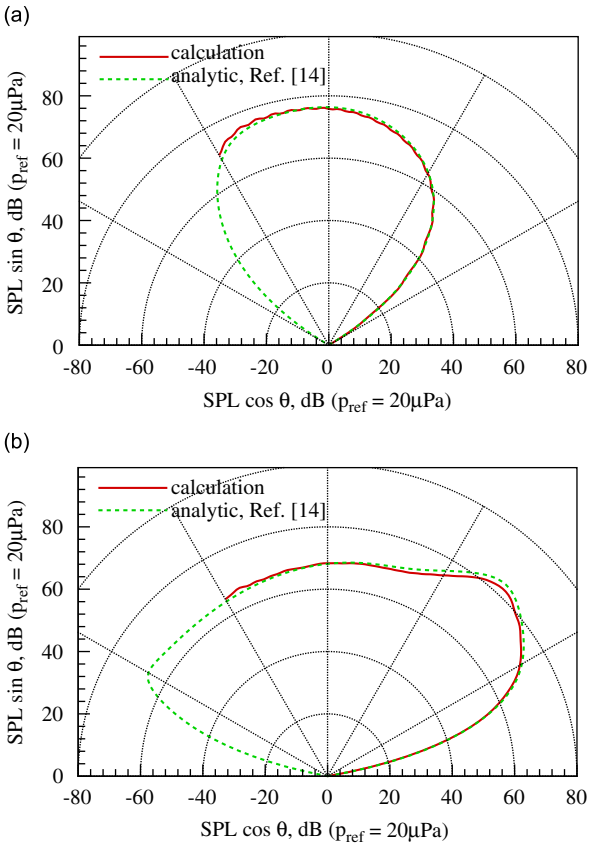

Fig. 18. Comparison of computed far-field sound pressure levels on a 46-m arc from the termination of Duct 2 passage with centerbody lined beyond the termination with $Z/\rho_b c_b = 2 - \mathrm{i}$, and the corresponding extended Munt's model solutions of Demir and Rienstra [14] at modes at $f = 866\,\mathrm{Hz}$, $M_\infty = 0.219$, $M_b = 0.447$, $kr_o = 19$. (a) (19,1) and (b) (10,1) modes.

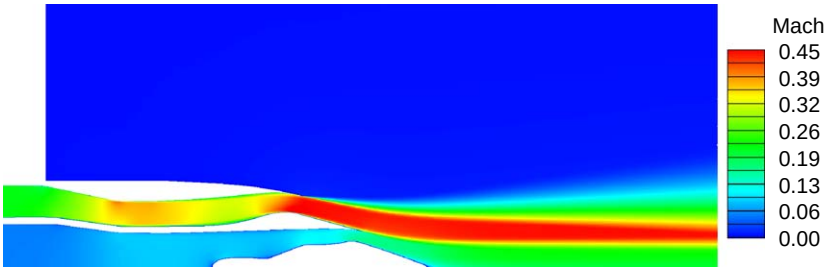

Fig. 19. Mean Mach number contours for the short cowl at static approach.

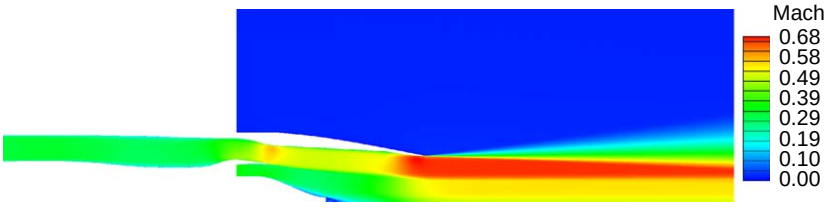

Fig. 20. Mean Mach number contours for the long cowl at static cutback.

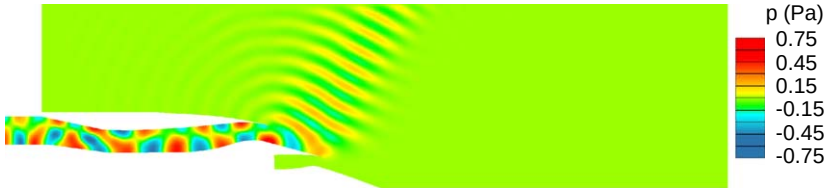

Fig. 21. Acoustic pressure contours for the (10,2) mode radiated from the short cowl at static approach and 8504 Hz.

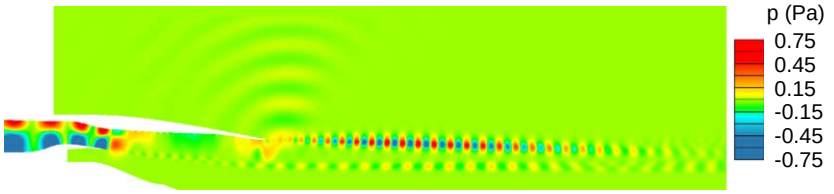

Fig. 22. Acoustic pressure contours for (9,2) mode radiated from the long cowl at static cutback and 5743 Hz.

mode carries three propagating radial modes, and the latter spinning mode carries two propagating radial modes at the indicated conditions. The mode amplitudes are specified according to the measurements. Also, the radial modes are combined according to their respective phases measured at the modal plane. The acoustic meshes are generated in a way to resolve the acoustic waves both through the ducts and the shear layers with more uniform distribution of the grid points than the CFD mesh. The CFD data are then interpolated to the acoustic mesh through linear interpolation.

Fig. 21 displays the computed radiation pattern for (10,2) mode from the short exhaust configuration, and Fig. 22 shows the radiated (9,2) mode from the long nacelle, as examples to the computed acoustic fields. The contour levels for both cases are displayed in such a way that the modes have unit pascal amplitudes at the modal planes in the bypass ducts. It is clear from Fig. 22 that some convective instabilities occur along the shear layer between the bypass jet and ambient region. However, as expected these instabilities seem to grow only gradually first and then decay as the shear layer grows. Comparisons with the measured far-field SPL data for the two cases are shown in Fig. 23a and b, respectively. Good agreement is evident from the figures for both cases.

4. Code performance and resource requirements

The above computations were done on a cluster of 12 PCs, each with a dual core Opteron processor and 4 GB of ram. One of the propagation and radiation cases with a dimensionless frequency of $kr_o = 31.2$ computed on a uniform 1501×501 mesh with about 3 million unknowns required approximately 62 GB of memory by the MUMPS [21] sparse solver. This exceeded the total memory of the system (48 GB), and the remaining memory need was supplied as virtual memory from the disk swap space. When the mesh is totally non-uniform, as in an actual engine, the memory need increases as the number of non-zero entries of the sparse coefficient matrix increases. The solution time remains quite small despite the size of the problem. Most of the above cases were solved in less than 30 min, including the far-field predictions. The longest time taking procedure was found to be the generation of appropriate grids.

5. Concluding remarks

In this paper a recently developed, direct, frequency-domain, linearized Euler solver, namely FLESTURN, has been described. Sound propagation studies were carried out through infinite ducts at different flow speeds and acoustic conditions using three different discretization algorithms. Propagation and radiation problems were solved for semi-infinite duct configurations at moderate and high velocities, assuming the duct and

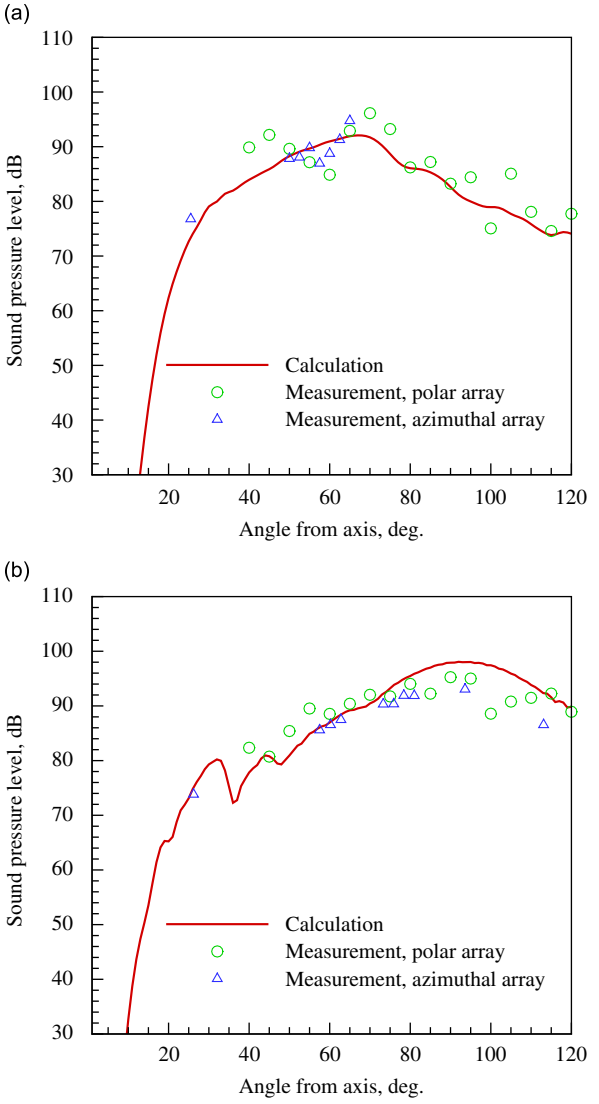

Fig. 23. Comparison of the computed and measured sound pressure levels for (a) $m = 10$ mode radiating from the short cowl at static approach and 8504 Hz and (b) $m = 9$ mode radiating from the long cowl at static cutback and 5743 Hz.

exterior flows were separated by an infinitely thin shear layer. Comparison of the hard-wall semi-infinite circular duct and both hard and soft semi-infinite annular duct results to the analytical solutions of Demir and Rienstra [14] indicated very good agreement. The developed code was also applied to realistic engine geometries at two different flow regimes, and the results were compared with experimental data with good agreement.

Acknowledgments

This work has been supported by the European Commission through the FP6 TURNEX project, coordinated by Brian J. Tester. Technical Officer for the project is Daniel Chiron. The author is grateful to the partners (a) Technische Universiteit Eindhoven (TUE) for providing the analytical results for the uniform cross-section duct cases, (b) industrial partners for acquiring and funding the experimental data, (c) Deutsches Zentrum für Luft- und Raumfahrt (DLR) for post-processing the measured data, (d) Institute of Sound and Vibration Research (ISVR) for performing the extensive validation work that enabled the comparisons with

the FLESTURN predictions to be illustrated herein, and (e) Rolls-Royce Deutschland (RRD) for providing the mean flow data for the long cowl. The author would also like to thank Kaan Koz for assisting in installation of the MUMPS sparse solver to the computing platform used.

References

[1] M.K. Myers, On the acoustic boundary condition in the presence of flow, *Journal of Sound and Vibration* 71 (3) (1980) 429–434.
[2] S.W. Rienstra, G.G. Vilenski, Spatial instability of boundary layer along impedance wall, in: *AIAA Paper* 2008-2932, 14*th AIAA/CEAS Aeroacoustics Conference*, Vancouver, Canada, May 2008.
[3] E.J. Brambley, Models for acoustically-lined turbofan ducts, in: *AIAA Paper* 2008-2879, 14*th AIAA/CEAS Aeroacoustics Conference*, Vancouver, Canada, May 2008.
[4] C.K.W. Tam, L. Auriault, Time-domain impedance conditions for computational aeroacoustics, *AIAA Journal* 34 (5) (1996) 917–923.
[5] Y. Özyörük, Parallel computation of forward radiated noise of ducted fans including acoustic treatment, *AIAA Journal* 40 (3) (2002) 450–455.
[6] S.W. Rienstra, Impedance models in time domain including the extended Helmholtz resonator model, in: *AIAA Paper* 2006-2686, 12*th AIAA/CEAS Aeroacoustics Conference*, Cambridge, Massachusetts, May 2006.
[7] A. Agarwal, P.J. Morris, R. Mani, The calculation of sound propagation in nonuniform flows: suppression of instability waves, in: *AIAA Paper* 2003-0878, 41*st Aerospace Sciences Meeting*, Reno, Nevada, January 2003.
[8] A. Michalke, Survey on jet instability theory, *Progress in Aerospace Sciences* 21 (1984) 159–199.
[9] J. Kok, Computation of sound radiation from cylindrical ducts with jets using a high-order finite-volume method, in: *AIAA Paper* 2007-3489, 13*th AIAA/CEAS Aeroacoustics Conference*, Rome, Italy, May 2007.
[10] J. Manera, B. Schiltz, R. Leneveu, S. Caro, J. Jacqmot, S. Rienstra, Kelvin–Helmholtz instabilities occurring at a nacelle exhaust, in: *AIAA Paper* 2008-2883, 14*th AIAA/CEAS Aeroacoustics Conference*, Vancouver, Canada, May 2008.
[11] X. Zhang, X.X. Chen, C.L. Morfey, P.A. Nelson, Computation of spinning modal radiation from an unflanged duct, *AIAA Journal* 42 (9) (2004) 1795–1801.
[12] R. Leneveu, B. Schiltz, S. Laldjee, S. Caro, Performance of a DGM scheme for LEE and applications to aircraft engine exhaust noise, in: *AIAA Paper* 2008-2884, 14*th AIAA/CEAS Aeroacoustics Conference*, Vancouver, Canada, May 2008.
[13] Y. Zhao, P.J. Morris, The prediction of fan exhaust noise propagation, in: *AIAA Paper* 2005-2815, 11*th AIAA/CEAS Aeroacoustics Conference*, Monterey, California, May 2005.
[14] A. Demir, S. Rienstra, Sound radiation from an annular duct with jet flow and a lined centerbody, in: *AIAA Paper* 2006-2718, 12*th AIAA Aeroaocoustics Conference*, Cambridge, MA, May, 2006.
[15] G. Gabard, R.J. Astley, Theoretical models for sound radiation from annular jet pipes: far- and near-field solutions, *Journal of Fluid Mechanics* 549 (2006) 315–342.
[16] R.M. Munt, The interation of sound with a subsonic jet issuing from a semi-infinite cylindrical pipe, *Journal of Fluid Mechanics* 4 (1977) 609–640.
[17] Q.F. Hu, A perfectly matched layer absorbing boundary condition for linearized Euler equations with a non-uniform mean flow, *Journal of Computational Physics* 208 (2005) 469–492.
[18] Y. Özyörük, E. Alpman, V. Ahuja, L.N. Long, Frequency-domain prediction of turbofan noise radiation, *Journal of Sound and Vibration* 270 (4–5) (2004) 933–950.
[19] F. Farassat, M.K. Myers, Extension of Kirchhoff's formula for radiation from moving surfaces, *Journal of Sound and Vibration* 123 (1988) 451–460.
[20] C.K.W. Tam, J.C. Webb, Dispersion-relation-preserving finite difference schemes for computational acoustics, *Journal of Computational Physics* 107 (1993) 262–281.
[21] ⟨http://mumps.enseeiht.fr/⟩, MUMPS: a MUltifrontal Massively Parallel sparse direct Solver.
[22] ⟨http://crd.lbl.gov/xiayoe/SuperLU⟩, SuperLU sparse matrix solver.
[23] R. Vichnevetsky, J.B. Bowles, *Fourier Analysis of Numerical Approximations of Hyperbolic Equations*, SIAM, Philadelphia, 1982.
[24] P.R. Amestoy, I.S. Duff, J.-Y.L. L'Excellent, Multifrontal parallel distributed symmetric and unsymmetric solvers, *Computer Methods in Applied Mechanics and Engineering* 184 (2000) 501–520.
[25] P.R. Amestoy, I.S. Duff, J.-Y.L. L'Excellent, J. Koster, A fully asynchronous multifrontal solver using distributed dynamic scheduling, *Journal on Matrix Analysis and Applications* 23 (2001) 15–41.
[26] P. Joseph, C.L. Morfey, C.R. Lowis, Multi-mode sound transmission in ducts with flow, *Journal of Sound and Vibration* 264 (2003) 523–544.
[27] F. Arnold, U. Tapken, R. Bauers, J. Zillmann, Turbomachinery exhaust noise radiation experiments—Part 1: polar directivity measurements, in: *AIAA Paper* 2008-2857, 14*th AIAA/CEAS Aeroacoustics Conference*, Vancouver, Canada, May 2008.
[28] U. Tapken, R. Bauers, F. Arnold, J. Zillmann, Turbomachinery exhaust noise radiation experiments—Part 2: in-duct and far-field mode analysis, in: *AIAA Paper* 2008-2858, 14*th AIAA/CEAS Aeroacoustics Conference*, Vancouver, Canada, May 2008.
[29] ⟨http://www.fluent.com/⟩, Computational Fluid Dynamics Modeling Software.